Chinese Chemical Letters 36 (2025) 110137

Contents lists available at ScienceDirect

Chinese Chemical Letters

journal homepage: www.elsevier.com/locate/cclet

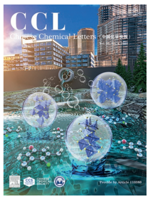

Design of highly active meso–zeolite enveloping Pt–Ni bimetallic catalysts for degradation of toluene

Tianyao He[a], Gan Li[a], Xiaoqiang Xie[a], Dong Han[a], Yunyue Leng[a], Qiuli Zhang[b], Wenming Liu[b], Guobo Li[a], Hongxiang Zhang[a], Shan Huang[a], Ting Huang[a], Honggen Peng[a,b,*]

[a] *School of Resources and Environment, Nanchang University, Nanchang 330031, China*
[b] *School of Chemistry and Chemical Engineering, Nanchang University, Nanchang 330031, China*

ARTICLE INFO

Article history:
Received 26 December 2023
Revised 5 June 2024
Accepted 17 June 2024
Available online 18 June 2024

Keywords:
Zeolite confinement effect
Pt–NiO interface
Toluene deep oxidation
Low temperature degradation
Reducing noble metal consumption

ABSTRACT

Degrading volatile organic compounds at low temperatures and active sites aggregation are still challenging. In this study, a novel mesoporous zeolite silicalite-1 (S-1–meso) enveloped Pt–Ni bimetallic catalysts (noted as Pt_1Ni_1@S-1–meso) were synthesized *via* a facile *in situ* mesoporous template-free method. The Pt–Ni bimetallic nanoparticles were uniformly distributed and displayed a large specific surface area and enriched mesopores to facilitate the deep oxidation of toluene. The presence of the Pt–NiO interface both increased the dispersion of the catalyst and improved its catalytic performance, thereby reducing the consumption of Pt. The Mars-van Krevelen mechanism and density function theory (DFT) calculations revealed that the Pt–NiO interface effect changed the electronic structure of Pt and Ni species, reduced the activation potential for oxygen, formed reactive oxygen species, and facilitated the adsorption and activation of reactants in the direction favorable to the toluene oxidation. This study provides a guideline for minimizing the proportion of precious metals used in practical applications and a promising method for toluene elimination at low temperatures.

The emission of volatile organic compounds (VOCs) has continuously increased in recent years [1,2]. Toluene as the most significant indoor air contaminant features a persistent aromatic ring structure and is frequently used as a solvent. Toluene is colorless and volatile, highly toxic to the environment, irritating to human skin and mucous membranes, and a cancer-causing agent to both humans and animals [3-6]. Therefore, eliminating the released toluene gas is vital.

Among the various VOC treatment technologies, catalytic combustion can degrade VOCs at a temperature of 200–400 °C [2,7-10]. Catalytic combustion features low energy consumption and treatment cost and does not generate secondary pollution and can degrade and eliminate all types of VOCs using a suitable catalyst. Therefore, catalytic combustion is a cheap and the most efficient method for VOCs treatment at this stage and displays a broad application prospect. Transition metal oxide catalysts and noble metal catalysts are commonly used catalysts for VOCs elimination *via* catalytic oxidation. These catalysts have limited applications owing to their high cost, scarce resources, and high surface energy of noble metal atoms, which tend to sinter and aggregate in the reaction, leading to deactivation and poor stability of the catalyst [11,12].

In recent decades, great efforts have been focused on investigating structure–property relationships to develop efficient and durable platinum-based catalysts [13-16]. Designing platinum metals with small particle sizes and high dispersions to enhance the interaction between metal and oxide supports is a widely used strategy for developing efficient and highly durable platinum-based catalysts [17]. As a commonly used precious metal support, zeolites feature a good microporous structure and excellent thermal stability and have attracted great interest in the adsorption and catalysis fields [18]. However, conventional loaded metals tend to develop into large particles at high temperatures, resulting in deactivation and growing costs because the Ostwald ripening process causes particle aggregation at high thermal reaction temperatures [19-21]. Catalyst deactivation under extreme conditions has been resolved through the development of a zeolite-supported metal catalyst (metal/zeolite) [22]. However, the microporous zeolite-confined catalysts still encountered several issues because ordinary zeolites typically feature pore sizes less than 2 nm, thereby limiting molecular diffusion and the accessibility of metal active sites

---

[*] Corresponding author.
E-mail address: penghonggen@ncu.edu.cn (H. Peng).

https://doi.org/10.1016/j.cclet.2024.110137

[8]. Therefore, improving the mass transfer efficiency of reactants and products and addressing the controllability of active centers on conventional-supported catalysts is a pressing issue. To solve this issue, mesoporous zeolite shells are constructed to increase the accessibility of active sites and the effectiveness of mass transfer [21,23,24]. Although numerous methods (including demetallization and soft–hard template methods) have been developed to generate mesopores in zeolites, it is still difficult to prepare zeolites with intracrystalline mesopores to limit active metal nanoparticles (NPs) simultaneously *via in situ* synthesis, because obtaining mesoporous zeolites remains difficult and cannot overcome several drawbacks such as high costs, health risks, restrictions on the zeolite synthesized, and reduced crystallinity of the zeolite [21,23,24].

Alternatively, the combination of platinum with other metal oxides is another efficient method used to reduce the number of noble metals owing to strong bimetallic synergies between metals [25-30]. Notably, the introduction of non-precious metal hydroxides to form polymetallic nanostructures can minimize the use of precious metals and improve catalytic performance. Although bimetallic catalysts have been widely reported and have achieved excellent catalytic performance in various non-homogeneous catalytic reactions, the mechanistic insights into the bimetallic synergistic properties and structure–property relationships are still unclear, mainly owing to the lack of precise modulation of catalyst structures (particularly bimetallic interfacial structures) [8,31]. Therefore, the precise design and construction of catalysts with specific structures are prerequisites for unraveling the bimetallic synergy and catalytic mechanisms.

In this study, single-crystal zeolite silicalite-1 (S-1) encapsulated Pt–Ni bimetallic NPs within mesopores (Pt_1Ni_1@S-1–meso) were synthesized *via* a simple *in situ* meso–temperate-free method, in contrast with ZSM-5, silicalite-1 shell has hydrophobic nature, owing to its high capacity for adsorbing VOCs, and high thermal durability, silicalite-1 zeolite has been widely used in catalytic processes [32]. The specific procedure for the preparation of Pt_1Ni_1@S-1–meso and related catalysts were described in Supporting information.

The X-Ray Diffraction (XRD) patterns of the Pt_1@SiO_2, Pt_2@SiO_2, Pt_1Ni_1@SiO_2, Pt_1Ni_1@S-1–meso, and Pt_1Ni_1/S-1 catalysts are displayed in Fig. S1 (Supporting information). The XRD pattern of Pt_1Ni_1@S-1–meso exhibited characteristic peaks corresponding to MFI zeolite structure, while that of Pt_1Ni_1@SiO_2 exhibited peaks corresponding to an amorphous silica (2θ range of 15°–35°) structure. The XRD pattern (JCPDS PDF #04–0802) of the standard platinum sample and (JCPDS PDF #47–1049) the nickel sample featured no diffraction signals associated with the Pt and Ni/NiO phases owing to their low loadings and high dispersions in the silicalite-1 zeolite shell. Thus, the loading of Pt and NiO/Ni did not induce a significant change in the crystal phase of silicalite-1.

Fig. S2 (Supporting information) shows the N_2 adsorption/desorption isotherms of the Pt_1@SiO_2, Pt_2@SiO_2, Pt_1Ni_1@SiO_2, and Pt_1Ni_1/S-1 samples. Pt_1@SiO_2, Pt_2@SiO_2, and Pt_1Ni_1@SiO_2 displayed a II-typed isotherm with a hysteresis loop in the relative pressure range of 0.8–1.0, indicating the presence of stacked mesopores in the isotherm. While Pt_1Ni_1/S-1 displayed an I-typed isotherm without mesopores. Moreover, Pt_1Ni_1@S-1–meso exhibited a typical I and IV-typed isotherm with an H3 hysteresis loop in the relative pressure range of 0.4–0.9, the pore size distribution in N_2 in a wide range of mesopores from 10 nm to 30 nm (Fig. S3 in Supporting information). The presence of mesopores over the Pt_1Ni_1@S-1–meso sample and the fabrication of hierarchical S-1 encasing Pt–Ni binary metal oxide active sites were both further supported by this study. The textural parameters of the samples are listed in Table S1 (Supporting information). The Pt_1Ni_1@S-1–meso sample featured a higher specific surface area (373 m^2/g) than the Pt_1Ni_1@SiO_2 precursor (73 m^2/g), which can improve toluene adsorption and extraction.

Figs. S4-S6 (Supporting information) depict the scanning electron microscopy (SEM), transmission electron microscopy (TEM) images, and particle size distributions of Pt_1@SiO_2, Pt_2@SiO_2, and Pt_1Ni_1@SiO_2, respectively, and also the morphologies of the catalysts. Pt/Pt–Ni enveloped in a silica shell featured microsphere particle sizes around 50 nm, and small Pt NPs displayed a mean size of around 1–2 nm. Fig. S7 (Supporting information) displays the morphology of Pt_1Ni_1@S-1–meso. The SEM (Fig. S7a), high-angle annular dark-field scanning transmission electron microscopy (HAADF-STEM) (Figs. S7b and c), and TEM (Fig. S7d) images indicate that silicalite-1 zeolites encapsulated the Pt_1Ni_1@S-1–meso material. The elemental line scan of Pt_1Ni_1@S-1–meso revealed that the Pt and Ni species were present in the hierarchical silicalite-1 shell (Figs. S6e and f). The energy dispersive X-ray spectroscopy (EDS)-mapping technique was used to analyze the spatial distribution of Pt and Ni species across the Pt_1Ni_1@S-1–meso sample. The results showed that both Pt and Ni species were uniformly distributed in the sample (Figs. S7g–l).

The aberration-corrected (AC)-TEM was further conducted to confirm the confinement of most Pt and Ni within a silicate-1 zeolite shell. Fig. 1 shows the encapsulation of Pt–Ni species in silicate-1 zeolite. The small black areas visible in Figs. 1a–c and the black areas visible in Figs. 1e and f showed the presence of partial mesopores inside the zeolite, indicating the synthesis of hierar-

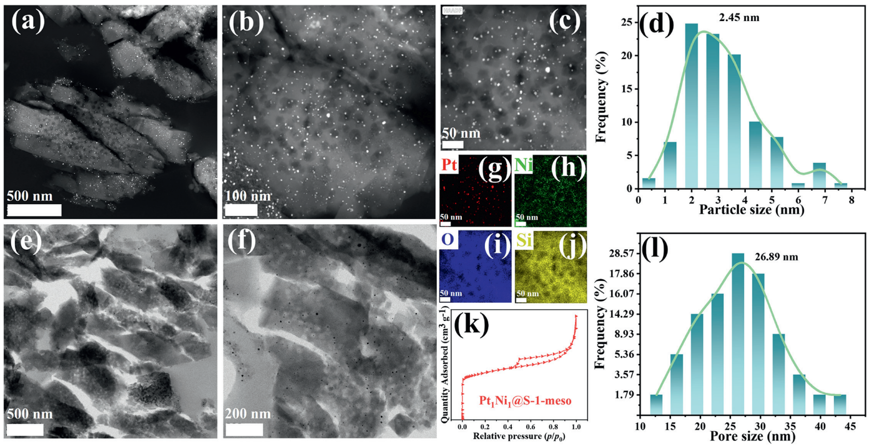

Fig. 1. (a–c) AC-dark field-TEM of Pt_1Ni_1@S-1–meso. (e, f) AC-bright field-TEM of Pt_1Ni_1@S-1–meso. (g–j) AC-EDS-mapping images of Pt_1Ni_1@S-1–meso. (k) N_2 adsorption/desorption isotherms Pt_1Ni_1@S-1–meso. (d) Particle size distribution Pt_1Ni_1@S-1–meso. (l) Pore size distribution of Pt_1Ni_1@S-1–meso.

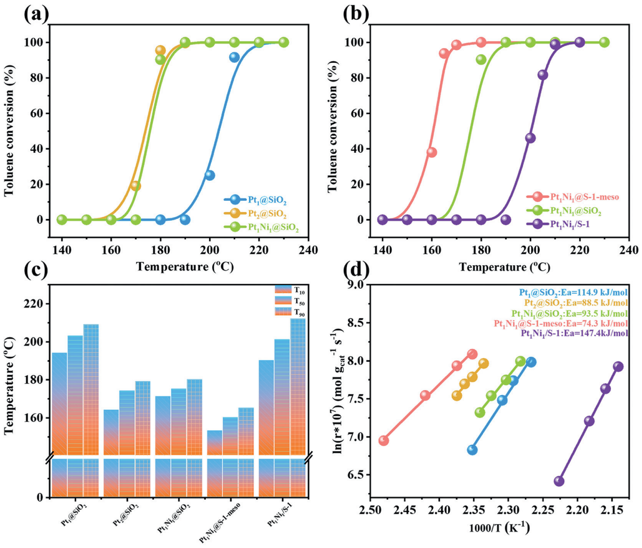

Fig. 2. (a, b) Catalytic activity of $Pt_1@SiO_2$, $Pt_2@SiO_2$, $Pt_1N_1@SiO_2$, Pt_1Ni_1/S-1, and $Pt_1Ni_1@S$-1–meso for the complete oxidation of toluene. (c) $T_{10\%}$, $T_{50\%}$, $T_{90\%}$ for the complete oxidation of toluene. Reaction conditions were 1000 ppm of toluene produced through bubbling with air, a total flow rate of 30 mL/min, and WHSV of 60,000 mL g^{-1} h^{-1}. (d) Arrhenius plots of $Pt_1Ni_1@S$-1–meso and related catalysts for the total toluene oxidation.

chical silicalite-1 containing intra-mesopores. Moreover, the intra-mesopores featured a mean particle size of ~2.5 nm, and a mean pore size of ~26.9 nm, consistent with Figs. 1d and l. In contrast, imaging of Pt_1Ni_1/S-1 samples showed that Pt–Ni were unevenly distributed on the exterior surface of the silicalite-1, Pt NPs displayed a size of about 4.0 nm, and Pt–Ni were supported on the margins of zeolites in these samples (Fig. S8 in Supporting information).

The toluene conversion over catalysts as a function of reaction temperature was conducted at a toluene concentration of 1000 ppm and weight hourly space velocity (WHSV) of 60,000 mL g^{-1} h^{-1}. The catalytic activities of $Pt_1@SiO_2$, $Pt_2@SiO_2$, $Pt_1Ni_1@SiO_2$, $Pt_1Ni_1@S$-1–meso, and Pt_1Ni_1/S-1 for toluene deep oxidation are presented in Figs. 2a and b. To facilitate the detailed toluene oxidation, the temperatures required for achieving 10%, 50%, and 90% of toluene conversion are summarized in Fig. 2c and Table S2 (Supporting information). The $Pt_1@SiO_2$, $Pt_2@SiO_2$, $Pt_1Ni_1@SiO_2$, $Pt_1Ni_1@S$-1–meso, and Pt_1Ni_1/S-1 exhibited 90% toluene conversion ($T_{90\%}$) at temperatures of 209, 179, 180, 165, and 212 °C, respectively. The $Pt_1Ni_1@S$-1–meso facilitated the full oxidation of toluene at the lowest $T_{100\%}$ value, indicating that $Pt_1Ni_1@S$-1–meso exhibited the highest catalytic activity among various catalysts and featured excellent performance than other catalysts reported in previous literature (Table S3 in Supporting information). Moreover, Fig. S9 (Supporting information) shows that the toluene conversion was greatly improved through the addition of a small amount of Pt. This improvement was probably attributable to the synergistic effect between platinum and nickel, the interaction, and the modulation of their electronic structures.

Moreover, the activation energy of the $Pt_1Ni_1@S$-1–meso series catalysts was calculated through changes in the catalytic activity and stability of toluene, and the effect of internal and external molecular diffusion was eliminated (Tables S4–S7 in Supporting information). Low conversion rates (<15%) and high WHSV (WHSV = 180,000 mL g^{-1} h^{-1}) were used to create the Arrhenius plots for toluene oxidation over these catalysts to exclude the mass transport limitation. $Pt_1Ni_1@S$-1–meso has the lowest reaction activation energy, which is consistent with the catalytic activity results (Fig. 2d). The results (Table S8 in Supporting information) showed that the Pt–NiO interface exhibited higher activity and turnover frequency (TOF) than bare Pt because $Pt_1Ni_1@SiO_2$ featured a higher catalytic activity than $Pt_1@SiO_2$. These results indicated that a suitable Pt–NiO interface as the main active site is vital for enhancing catalytic activity.

The catalytic testing of CO_2 and water vapor resistance over $Pt_1Ni_1@S$-1–meso is displayed in Figs. S10a and b (Supporting information). After the addition of 5 vol% H_2O and 10 vol% CO_2 separately, the $Pt_1Ni_1@S$-1–meso featured a higher catalytic activity. The results showed that $Pt_1Ni_1@S$-1–meso was impervious to H_2O and CO_2 owing to the protective properties of zeolite shells, which hinder the direct penetration of active ingredients into these compounds. We performed FT-IR profile of $Pt_1Ni_1@S$-1–meso and S-1–meso, and multiple vibrational peaks appeared in the range of 250–1500 for these samples in Fig. S11 (Supporting information). The peaks at the positions of 1227 and 804 cm^{-1} are attributed to the internal vibrations of the SiO_4 tetrahedra, specifically the O-Si-O The three peaks at position 557 cm^{-1} are attributed to the external vibrations of the SiO_4 tetrahedra, and the vibrational peak appearing at 1082 cm^{-1} is attributed to the stretching vibrations of Si-O in Si-OH.

After being treated at 162 °C for 100 h, $Pt_1Ni_1@S$-1–meso featured a slight decrease in catalytic efficiency (Fig. S10c). In addition, the toluene conversion curves against temperature spanning after 10 successive trials, with an excellent curve overlap, indicated that the catalyst was stable even after 10 recycles (Fig. S10d). Therefore, the excellent stability of catalysts in terms of geometry and structure facilitates their catalytic performance during toluene combustion. These results indicated that $Pt_1Ni_1@S$-1–meso displayed good industrial applications. During stability have added catalytic testing of water and CO_2 resistance in Fig. S12 (Supporting information), no significant decrease in catalyst activity occurred with the introduction of 3 vol% water vapor and 10% CO_2. To elucidate its higher catalytic stability, the exhausted catalyst was characterized *via* Raman spectroscopy. The Raman spectra (Fig. S13 in Supporting information) of the catalyst featured no peaks related to carbon impurities.

Thermal stability tests were conducted to evaluate the anti-sintering performance of $Pt_1Ni_1@S$-1–meso, Pt_1Ni_1/S-1–meso, and Pt_1Ni_1/S-1 (Fig. S14a in Supporting information). $Pt_1Ni_1@S$-1–meso-700 °C and Pt_1Ni_1/S-1–700 °C were samples subjected to a two-hour high-temperature treatment in nitrogen at 700 °C. $Pt_1Ni_1@S$-1–meso-700 °C featured no reduction in catalytic activity compared with a $Pt_1Ni_1@S$-1–meso fresh sample. However, compared with the freshly prepared sample, the activity of the traditionally supported Pt_1Ni_1/S-1–700 °C catalyst significantly decreased. The Raman patterns (Fig. S14b in Supporting information) of Pt_1Ni_1/S-1–meso featured impurity peaks of carbon. The XRD patterns of $Pt_1Ni_1@S$-1–meso-700 °C and Pt_1Ni_1/S-1–700 °C are shown in Figs. S14c and d (Supporting information). The XRD pattern of thermally treated $Pt_1Ni_1@S$-1–meso-700 °C did not exhibit Pt diffraction peaks. However, the Pt_1Ni_1/S-1–700 °C exhibited a higher Pt diffraction intensity than the freshly reduced Pt_1Ni_1/S-1 sample. These results showed that $Pt_1Ni_1@S$-1–meso featured good thermal stability, which can be attributable to the confinement effect of the S-1 shell, thereby hindering the aggregation of Pt–Ni NPs.

The migration of metal nanoparticles within the zeolite was inhibited owing to the confinement effect of zeolites and the enhanced Pt–NiO interfacial interaction. After a high-temperature treatment in nitrogen at 700 °C for 2 h, Pt–Ni species of $Pt_1Ni_1@S$-1–meso were still significantly confined in the intra-mesopores and could not agglomerate (Figs. S15a and b in Supporting information). In contrast, the Pt–Ni species of Pt_1Ni_1/S-1 after a high-temperature treatment at 700 °C for 2 h in nitrogen featured large agglomerates with an increased particle size from 4.0 nm to

11.2 nm (Fig. S16 in Supporting information) compared with the Pt_1Ni_1/S-1 fresh sample (Fig. S8). These results demonstrated that Pt_1Ni_1@S-1–meso exhibited excellent long-term thermal stability and high performance for inhibiting deactivations in industrial applications. The large particle size of the Pt_1Ni_1@S-1–meso sample hindered particle migration, coalescence, and Ostwald ripening after rigorous treatment (Fig. S15 in Supporting information). The limited particle migration can effectively solve issues such as particle aggregation at high temperatures [20,26,33-36].

The hydrogen temperature-programmed reduction (H_2-TPR) test was performed to explore the reducibility of all Pt–NiO samples (Fig. S17a in Supporting information). The Ni@S-1–meso catalyst featured two distinct hydrogen consumption peaks, corresponding to NiO reduction, but the external surface reduction of Ni^{2+} to Ni correlated with the reduction peak at 155 °C, and displayed reduction peaks at 685 °C, corresponding to the reduction of Ni^{2+} to Ni within the bulk phase [37]. The H_2 spillover effect on the Pt_1Ni_1@S-1–meso catalyst caused the peaks at 685 °C to shift to a lower temperature, less than 669 °C, after the addition of Pt species, owing to the hydrogen spillover from Pt to NiO [29]. This phenomenon confirmed the existence of the Pt–NiO interface, indicating the electron transfer from NiO to Pt. Furthermore, the oxygen analysis revealed that the oxygen temperature programmed desorption (O_2-TPD) curves comprised surface-adsorbed oxygen species (below 200 °C), surface lattice oxygen species (between 200 °C and 400 °C), and bulk lattice oxygen (above 400 °C) (Fig. S17b in Supporting information) [19,31,38]. After the introduction of the Pt–NiO interface, the reactive oxygen species significantly increased. Generally, oxygen species play a significant role in oxidation reactions as the primary reactive oxygen species [38].

The X-ray photoelectron spectroscopy (XPS) analysis was performed to evaluate the surface oxidation states of Pt and Ni species and the Pt–NiO interface effect (Figs. S17c and d in Supporting information), and the surface compositions of all catalysts determined from XPS data are listed in Table S9 (Supporting information). The XPS spectra of $Pt_1@SiO_2$ and $Pt_1Ni_1@SiO_2$ samples featured no clear signals (Fig. S17c), confirming the TEM results, which indicates that practically all platinum nanoparticles are trapped within the SiO_2 shell. The Pt $4f_{7/2}$ spectra of Pt^0 and Pt^{2+} featured binding energy around 71.1 and 72.4 eV, respectively [5]. The Pt $4f_{7/2}$ XPS spectra of $Pt_1@SiO_2$ catalysts exhibited a peak at 72.4 eV, corresponding to Pt^0, while those of the $Pt_1@SiO_2$ catalysts featured a peak at 75.2 eV, corresponding to Pt^{2+}. The strong metal-support interaction can influence the electronic and catalytic characteristics of the Pt surface [39]. However, the $Pt_1Ni_1@SiO_2$ catalysts featured a significant peak shift from 72.0 eV to 73.9 eV, indicating that Pt species were fully reduced into a metallic state owing to electron transfer effects between platinum and nickel, thus the metallic Pt rather than cationic Pt provided active sites for toluene oxidation [40]. The nickel species as an electron donor can enhance the electron density of encapsulated Pt species. In addition, $Pt_1Ni_1@SiO_2$ displayed higher surface $Pt^0/(Pt^0+Pt^{2+})$ ratio, consistent with the H_2-TPR results [37,40]. The Pt $4f_{7/2}$ XPS spectra of Pt_1Ni_1@S-1–meso catalysts exhibited peaks at 71.8 and 73.5 eV, respectively. In contrast, the peaks of $Pt_1Ni_1@SiO_2$ catalysts negatively shifted from 0.2 eV to 0.4 eV, which may be attributable to metal-support interactions [41]. Pt species can exist in higher chemical states as a result of greater interactions between smaller nanoparticles of platinum and zeolite carriers [41].

Through the XPS analysis, the chemical states of Ni species present in zeolites were also assessed. The XPS spectra of the Pt_1Ni_1@S-1–meso sample (Fig. S17d and Table S9 Supporting information) displayed two main peaks with binding energy values of 857.3 and 875.0 eV, corresponding to $2p_{3/2}$ and $2p_{1/2}$ of nickel oxide phase, respectively [42]. This indicated that the Ni encapsulated in the pore channel cannot be reduced at 400 °C, exists in the form of NiO, and is present at the Pt–NiO interface, consistent with the H_2-TPR results. Compared with $Pt_1Ni_1@SiO_2$, the binding energy values of encapsulated zeolites shifted from 0.1 eV to 0.5 eV owing to the zeolite framework [41].

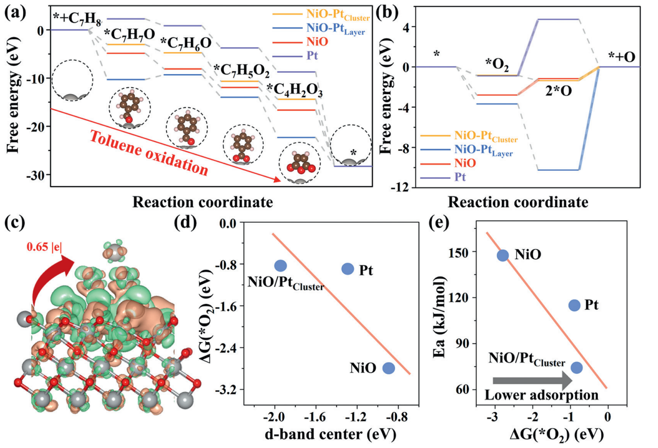

Fig. 3. (a) the free energy profile of toluene oxidation on active Pt/Ni atoms. (b) The free energy profile of O_2 dissociation into free radical O^- on active Pt/Ni atoms. (c) Charge density difference. (d) The correlation between $^*O_2$ adsorption energy ($\Delta G_{^*O_2}$) and d-band center of average Ni/Pt atoms. (e) volcano-shaped relationship between experimental E_a and calculated $^*O_2$ adsorption energy ($\Delta G_{^*O_2}$).

The X-ray absorption near-edge structure (XANES) and X-ray absorption fine structure (EXAFS) were used to obtain detailed electronic and structural information of the Pt and Ni species in Pt_1Ni_1@S-1–meso. The Pt L_3-edge XANES spectra (Fig. 3 and Fig. S18 in Supporting information) of Pt_1Ni_1@S-1–meso and the Pt foil reference spectra were comparable, indicating that the metal Pt^0 species are the predominant Pt species. However, some differences existed in the spectra of both catalysts, which are mainly attributable to the size of the metal clusters [42,43]. Significantly, the XPS spectra of Pt 4f and Ni 2p revealed that the Pt and Ni species featured a metallic valence of +2, respectively. The Pt_1Ni_1@S-1–meso displayed a smaller shift of the Ni K-edge absorption toward higher binding energy compared with NiO, indicating that the Pt atoms in Pt_1Ni_1@S-1–meso exhibited a higher electron density and the presence of Ni species led to charge transfer from Ni to Pt, thereby forming an electron-enriched surface of Pt NPs and Pt–NiO interface in Pt_1Ni_1@S-1–meso, consistent with XPS and H_2-TPR results [44]. The Pt L_3-edge Fourier-transformed EXAFS spectra of Pt_1Ni_1@S-1–meso (Fig. 3c, Fig. S19f and Table S10 in Supporting information) featured Pt–O, Pt–Pt, and Pt–Ni bonds with lengths of 2.206, 2.755, and 3.350 Å, respectively. The Ni K-edge Fourier-transformed EXAFS spectra of Pt_1Ni_1@S-1–meso (Fig. 3d, Fig. S20f, and Table S10 in Supporting information) exhibited Ni–O and Ni–Ni bonds, with lengths of 2.054 and 3.085 Å, respectively [42]. Additionally, the bond lengths of Ni–O (~2.054 Å) over Pt_1Ni_1@S-1–meso were slightly shorter than those of NiO (~2.089 Å), while the bond lengths of Ni–Ni (~3.085 Å) over Pt_1Ni_1@S-1–meso catalysts were slightly longer than those of Ni foil (~2.484 Å), indicating a higher electron density of Pt atoms in Pt_1Ni_1@S-1–meso (Table S10). The wavelet transform plot showed that the signal intensities of Pt–Pt in Pt_1Ni_1@S-1–meso were stronger and broader than those of Pt foil at $R + \Delta R$ ~ 2.0–3.0 Å, while those of Ni–O in Pt_1Ni_1@S-1–meso were weaker and broader than in NiO at $R + \Delta R$ ~ 1.0–2.0 Å (Fig. 3h). Consequently, the results of XPS, H_2-TPR, XANES, EXAFS, and wavelet transform plots indicated that the Pt–NiO interface between Pt and the Ni overlayer on Pt_1Ni_1@S-1–meso was created. The Pt–NiO interface improved charge transfer from NiO to Pt and formed an electron-rich surface for Pt NPs, thereby providing new active sites to enhance catalytic effectiveness.

To explore the enhanced catalytic performance of the Pt–NiO bimetal catalyst, density function theory (DFT) calculations were conducted to investigate the catalytic toluene oxidation. NiO, Pt, NiO/$Pt_{Cluster}$, and Ni/Pt_{Layer} were modeled to stimulate the catalysts used in the above experiment. The catalytic process was investigated on Ni/Pt atoms in these catalysts, and the corresponding free energy change was calculated and displayed in Fig. 3a. The toluene oxidation is mainly a spontaneous and exothermic process accompanied by the downshifted energy change. Furthermore, the conversion of C_7H_8 into C_7H_7O over Pt catalysts required high energy input to overcome barriers. Thus, with sufficient free radicals, the toluene oxidation could easily proceed on NiO, Pt, and Pt/NiO. Consequently, the O_2 conversion into free radicals was further investigated (Fig. 3b). Generally, the maximal energy increase is the rate-determining step (RDS), which determines the difficulty associated with the catalytic reaction. The $^*O_2$ dissolution into 2^*O on Pt and NiO is RDS with a ΔG_{RDS} of 5.62 and 1.63 eV, respectively, while the $^*O$ desorption on NiO/$Pt_{Cluster}$ and Ni/Pt_{Layer} is the key step with ΔG_{RDS} of 1.37 and 10.25 eV, respectively. This indicated that NiO/$Pt_{Cluster}$ displayed higher catalytic activity than Pt and NiO, consistent with experimental results.

Furthermore, we calculated the electronic structures to elucidate the enhanced toluene degradation mechanism. The charge density difference (Fig. 3c) indicated that the electron assembled on the interface between Ni and Pt layers, which confirms the presence of strong interaction, mediates the electronic structure of Pt layers. Fig. 3d displays a decreased $\Delta G_{^*O_2}$ with an increased D-band center, clarifying the regulation effect of the NiO layer on the NiO/$Pt_{Cluster}$. More importantly, Fig. 3e shows a volcano-shaped relationship between experimental E_a and calculated $\Delta G_{^*O_2}$. This indicated that the decreased $^*O_2$ adsorption energy promoted lower E_a for the preceding reaction. Comparably, NiO/$Pt_{Cluster}$ exhibited relatively mild adsorption and consequently a lower E_a, which can further promote the O_2 dissolution and toluene oxidation. Therefore, the performance of NiO/$Pt_{Cluster}$ is enhanced through the dissolution process of the adsorbed O_2, thereby providing sufficient O^- free radicals to accelerate toluene oxidation.

Fig. S21 (Supporting information) displays the *in-situ* DRIFTS of the Pt_1Ni_1@S-1–meso catalyst under oxygen-enriched conditions. Table S11 (Supporting information) displays the matching infrared vibration data of the intermediate species. The intermediate species (benzyl alcohol, benzaldehyde, benzoic acid, maleic anhydride, and carbonate) were accumulated on the surface of the Pt_1Ni_1@S-1–meso catalyst, and the ring-opening process of benzoate intermediates showed the further oxidation of benzoic acid into maleic anhydride, which is usually the rate-determining step for catalytic toluene decomposition [6,9,45].

In addition, the *in-situ* DRIFTS was performed to further study the process of catalytic toluene oxidation over the Pt_1Ni_1@S-1–meso catalyst. The toluene adsorption process was conducted at 50 °C, and the results are shown in Fig. S22 (Supporting information). The *in-situ* DRIFTS of the Pt_1Ni_1@S-1–meso catalyst featured spectral bands at 3059, 3028, 2970, and 2927 cm^{-1}, which can be attributable to ν(C–O), $\delta_{as}(CH_3)$, $\delta_s(CH_3)$, and ν(C–C) of the adsorbed toluene, respectively [7,17]. Moreover, the intensity of each different peak rapidly increased over a short period and nearly reached adsorption saturation, indicating that toluene molecules can easily bind to the Pt_1Ni_1@S-1–meso catalyst, which supports the subsequent redox process. The catalytic combustion of toluene in the presence of gas-phase oxygen was investigated. The spectra of the Pt_1Ni_1@S-1–meso catalyst featured new peaks, indicating the partial oxidation of toluene. In addition, some new peaks at 1647–1883 and 1340–1565 cm^{-1} corresponded to the $\nu_{as}(CO_3{}^{2-})$ peak of carbonate, indicating the total combustion of toluene [6,10].

In contrast to the oxygen-enriched conditions, the toluene adsorption process was conducted at 162 °C, resulting in a continuous increase in the accumulation of benzoate under anoxic conditions (Fig. S23 in Supporting information). The toluene adsorption reflected the depletion of lattice oxygen under anoxic conditions, indicating a deep involvement of surface-adsorbed oxygen and lattice oxygen species in toluene oxidation under the absence of gaseous oxygen. The hydroxyl peak was replenished through the introduction of 20% $O_2 + 90\%$ N_2, therefore, gas-phase oxygen is activated under oxygen-enriched conditions to reduce the lattice oxygen consumption. The sufficient reactive oxygen species could continuously degrade toluene, leading to the formation of intermediate species. At the initial stage, the benzoic acid featured a stable accumulation, indicating a high performance of oxygen species on the Pt surface. The accumulation of benzoate increased with time, indicating high mobility of lattice oxygen in toluene combustion, even though insufficient reactive oxygen species could not facilitate the ring-opening process of benzoic acid into maleic anhydride. The characteristic peak intensity of toluene (3059, 3028, 2927, and 2870 cm^{-1}) rapidly decreased under the presence of gas-phase oxygen. Under oxygen conditions, the intensity of toluene peaks at 170 and 210 °C were significantly lower than those in the absence of oxygen. Therefore, the Mars-van Krevelen (MvK) mechanism governs the catalytic combustion of toluene over the Pt_1Ni_1@S-1–meso catalyst. The intensity of the 1572 cm^{-1} peak corresponding to maleic anhydride species increased at higher temperatures in the presence of oxygen, indicating that toluene has undergone extensive oxidation.

The proposed toluene degradation mechanism over the Pt_1Ni_1@S-1–meso catalyst was based on the aforementioned procedure. The electron transport effect between Pt and Ni species may be the key factor affecting their catalytic performance, and these species were typically regarded as active toluene decomposition sites. At the active sites, toluene was adsorbed and then reacted with reactive oxygen species to produce intermediates. Through the electron absorption from the electron-rich Pt species, electrophilic O_2 molecules were activated, thereby forming nucleophilic oxygen species in combination with toluene to restore the depleted lattice oxygen.

In summary, the Pt_1Ni_1@S-1–meso catalyst exhibited the highest catalytic performance for toluene oxidation owing to the confinement effect of mesoporous zeolite shell and the suitable Pt–Ni bimetallic synergistic effect. The Pt–NiO interface provided new active sites for enhancing the electron transfer from Ni to Pt, which forms reactive species for oxygen resolution and toluene oxidation. According to the XPS, O_2-TPD, H_2-TPR, XANES, EXAFS, DFT calculations, and *in-situ* DRIFTS analysis of toluene oxidation on Pt_1Ni_1@S-1–meso, a potential catalytic MvK mechanism was postulated. Toluene was adsorbed on a Pt_1Ni_1@S-1–meso catalyst containing a little additional amount of Ni. The Ni addition can facilitate the toluene adsorption process and improve the interaction between toluene and the active phase. After a sequence of redox reactions with the catalyst oxygen species, the adsorbed toluene was oxidized to innocuous gas-phase CO_2 and H_2O. Toluene degradation was significantly accelerated under the presence of gas-phase oxygen through the addition of reactive oxygen species. Finally, the catalyst degraded toluene into H_2O and CO_2. This study provides guidelines for degrading VOCs at a low temperature and reducing the consumption of noble metals.

Declaration of competing interest

The authors declare that they have no known competing financial interests or personal relationships that could have appeared to influence the work reported in this paper.

CRediT authorship contribution statement

Tianyao He: Writing – review & editing, Writing – original draft, Investigation, Conceptualization. **Gan Li:** Investigation. **Xiaoqiang Xie:** Conceptualization. **Dong Han:** Investigation. **Yunyue Leng:** Investigation. **Qiuli Zhang:** Investigation. **Wenming Liu:** Methodology. **Guobo Li:** Writing – review & editing, Methodology. **Hongxiang Zhang:** Methodology. **Shan Huang:** Methodology. **Ting Huang:** Methodology. **Honggen Peng:** Writing – review & editing, Writing – original draft, Project administration, Investigation, Funding acquisition, Conceptualization.

Acknowledgments

This work was supported by the National Natural Science Foundation of China (Nos. 22276086, 21976078), the Natural Science Foundation of Jiangxi Province (Nos. 20202ACB213001, 20232BCJ22003), all of which are greatly acknowledged by the authors.

Supplementary materials

Supplementary material associated with this article can be found, in the online version, at doi:10.1016/j.cclet.2024.110137.

References

[1] Q. Gao, L. Sun, Z. Wang, et al., Chin. Chem. Lett. 35 (2024) 109255.
[2] M. Qi, Z. Li, Z. Zhang, et al., Chin. Chem. Lett. 34 (2023) 107437.
[3] Y. Guo, M. Wen, G. Li, et al., Appl. Catal. B: Environ. 281 (2021) 119447.
[4] C. He, J. Cheng, X. Zhang, et al., Chem. Rev. 119 (2019) 4471–4568.
[5] R. Peng, S. Li, X. Sun, et al., Appl. Catal. B: Environ. 220 (2018) 462–470.
[6] Z. Su, W. Yang, C. Wang, et al., Environ. Sci. Technol. 54 (2020) 12684–12692.
[7] C. Dong, H. Wang, Y. Ren, et al., J. Environ. Sci. 104 (2021) 102–112.
[8] J. He, D. Chen, N. Li, et al., Appl. Catal. B: Environ. 265 (2020) 118560.
[9] Y. Shen, J. Deng, S. Impeng, et al., Environ. Sci. Technol. 54 (2020) 10342–10350.
[10] W. Yang, Y. Peng, Y. Wang, et al., Appl. Catal. B: Environ. 278 (2020) 119279.
[11] N. Fu, X. Liang, X. Wang, et al., J. Am. Chem. Soc. 145 (2023) 9540–9547.
[12] N. Ye, J. Zheng, K. Xie, et al., J. Rare Earths 41 (2023) 889–895.
[13] T. He, W. Wang, F. Shi, et al., Nature 598 (2021) 76–81.
[14] Y. Ma, A.N. Kuhn, W. Gao, et al., Nano Energy 79 (2021) 105465.
[15] Y. Yang, I.B. Perry, G. Lu, et al., Science 353 (2016) 144–150.
[16] S. Ye, F. Luo, Q. Zhang, et al., Energy Environ. Sci. 12 (2019) 1000–1007.
[17] Z. Wang, H. Yang, R. Liu, et al., J. Hazard. Mater. 392 (2020) 122258.
[18] M. Song, E. Eom, J.W. Shin, et al., Angew. Chem. Int. Ed. 62 (2023) e202303503.
[19] X. Fu, Y. Liu, J. Deng, et al., Appl. Catal. A: Gen. 595 (2020) 117509.
[20] S. Hu, W.X. Li, Science 374 (2021) 1360–1365.
[21] H. Peng, T. Dong, S. Yang, et al., Nat. Commun. 13 (2022) 13–295.
[22] L. Wei, Y. Liu, S. Cui, et al., Adv. Funct. Mater. 33 (2023) 2306129.
[23] R. Ryoo, Nature 575 (2019) 40–41.
[24] D. Zhao, J. Feng, Q. Huo, et al., Science 279 (1998) 548–552.
[25] C. Hohner, M. Ronovský, O. Brummel, et al., J. Catal. 398 (2021) 171–184.
[26] S. Liu, Y. Li, X. Yu, et al., Nat. Commun. 13 (2022) 1–10.
[27] Y. Shi, Z. Li, J. Wang, et al., Appl. Catal. B: Environ. 286 (2021) 119936.
[28] Y. Su, K. Fu, Y. Zheng, et al., Appl. Catal. B: Environ. 288 (2021) 119980.
[29] M. Xiao, X. Yu, Y. Guo, et al., Environ. Sci. Technol. 56 (2022) 1376–1385.
[30] J. Xie, H. Jiang, S. Guo, A.C.S. Appl. Nano Mater. 4 (2021) 3044–3051.
[31] L. Yang, Q. Liu, R. Han, et al., Appl. Catal. B: Environ. 309 (2022) 121224.
[32] M. Javed, S. Cheng, G. Zhang, et al., Fuel 215 (2018) 226–231.
[33] T. Otto, S.I. Zones, E. Iglesia, J. Catal. 339 (2016) 195–208.
[34] T. Otto, J.M. Ramallo-López, L.J. Giovanetti, et al., J. Catal. 342 (2016) 125–137.
[35] N. Wang, Q. Sun, J. Yu, Adv. Mater. 31 (2019) 1803966.
[36] Z. Wu, S. Goel, M. Choi, et al., J. Catal. 311 (2014) 458–468.
[37] L. Li, A. Cheruvathur, S. Zuo, et al., Appl. Catal. B: Environ. 299 (2021) 120670.
[38] X. Liu, J. Mi, L. Shi, et al., Angew. Chem. Int. Ed. 60 (2021) 26747–26754.
[39] H. Huang, D.Y.C. Leung, J. Catal. 280 (2011) 60–67.
[40] Q. Feng, X. Wang, M. Klingenhof, et al., Angew. Chem. Int. Ed. 61 (2022) e202203728.
[41] C. Chen, F. Chen, L. Zhang, et al., Chem. Commun. 51 (2015) 5936–5938.
[42] P. Yan, S. Xi, H. Peng, et al., J. Am. Chem. Soc. 145 (2023) 9718–9728.
[43] Q. Sun, B.W.J. Chen, N. Wang, et al., Angew. Chem. Int. Ed. 59 (2020) 20183–20191.
[44] J. Xu, Y. Wang, K. Wang, et al., Angew. Chem. Int. Ed. 62 (2023) e202302877.
[45] S. Mo, J. Li, R. Liao, et al., Chem. Eng. J. 418 (2021) 129399.